

Characterising the Nature of Diffusion via a New Indicator: Microcylinder and Microring Electrodes

Haonan Le, Enno Kätelhön, and Richard G. Compton*

Department of Chemistry, Physical and Theoretical Chemistry Laboratory, Oxford University
South Parks Road, Oxford, OX1 3QZ, United Kingdom

Abstract

An indicator to character diffusion is introduced to quantify the extent of linear and convergent diffusion in chronoamperometric currents. Simulated data for microcylinder and microring models is thus characterised and different time scales of diffusive fluxes from different spatial locations are revealed and discussed. Finally, the applicability of the Aoki equation [*Journal of Electroanalytical Chemistry*, **186**, 79 (1985)] to the chronoamperometric currents for various cylinder-like models is explored and assessed.

1 Introduction

Microelectrodes are of great importance to electrochemical studies of mass transport, reaction mechanisms and voltammetry as reviewed in the literature^{1–7}. In particular, diffusion can be readily studied through microcylinder electrodes and microwire electrodes^{8–32} due to their ease of fabrication and utilisation. The theoretical studies of diffusive fluxes towards microcylinder electrodes by Aoki et al⁸ and Szabo et al¹¹ reported two approximate equations in 1985 and 1987, respectively, to describe the chronoamperometric currents towards infinitely long cylindrical electrodes. In 2009, Fang et al¹⁸ proposed a different approximate equation which features a simpler form.

The simulation of more complex cylinder-like systems started later. Ferrigno et al¹⁶ reported in 1997 numerical simulations of a ‘protruding microdisc’ model and discussed the influence of the protruding cylinder-like part of the electrode on the total current. Dickinson et al¹⁷ reported simulations of ‘top-only’ and ‘side-only’ cylindrical electrode models with only the top or the side of the cylinder being

*Corresponding author: Richard G. Compton, richard.compton@chem.ox.ac.uk

electrochemical active and presented a brief analysis of the partial derivative of current with respect to time in Log_{10} scales, on which basis we below develop the diffusion indicator α . Britz et al²⁰ reported a comparison between the chronoamperometric currents at a infinitely long cylindrical electrode and a capped cylindrical electrode in 2010 and discuss the (quasi-) steady-state currents in these two models with respect to the length of the cylindrical electrode. Bieniasz has published studies^{21–23} to provide various simulation methods for cylindrical electrodes.

In this study, we introduce a new characterisation indicator for diffusion, the diffusion indicator α , and use it to analyse simulated chronoamperometric data of cylinder-like electrode models. In addition, we include an analysis of a microring model.

2 Simulation Methods

In this section, our theoretical models are presented in detail followed by the introduction of dimensionless parameters and the computational methods used in this work.

2.1 Theoretical Models

We model potential step chronoamperometry of a cylindrical wire electrode geometry considering two different situations as shown in ① and ② in Figure 1. The first model, the ‘annular band’ electrode model, is an infinite cylinder featuring an electrochemically active area in the shape of an annular band on an otherwise insulating surface. The second model is a capped cylinder electrode, the ‘full cylinder’ electrode model, with two variations of this model: the ‘side-active-only cylinder’ electrode model, and the ‘end-active-only cylinder’ electrode model. To obtain a better understanding of the diffusion mechanism of the analyte during electrochemical reactions in these two models, we further model the chronoamperometry in an electrode geometry where a ring-shape electrode is embedded on a surface, the ‘embedded ring’ electrode model, as shown in ③ in Figure 1. More detailed reasons for using the latter model are explained later in this paper.

In all three models, the initial concentrations c^* of the analyte A are uniform before the reaction starts. After applying a sufficiently large overpotential (‘potential step chronoamperometry’) at the electrochemically active area, A is reduced at the solution-electrode interface where the single-electron-transfer reaction $A + e \rightarrow B$ takes place. Assuming a sufficiently large overpotential at the electrode and sufficient electrolyte concentration, the reaction of analyte is considered to be diffusion-controlled. By varying the sizes of the electrochemically active areas, the time evolution of the currents and the

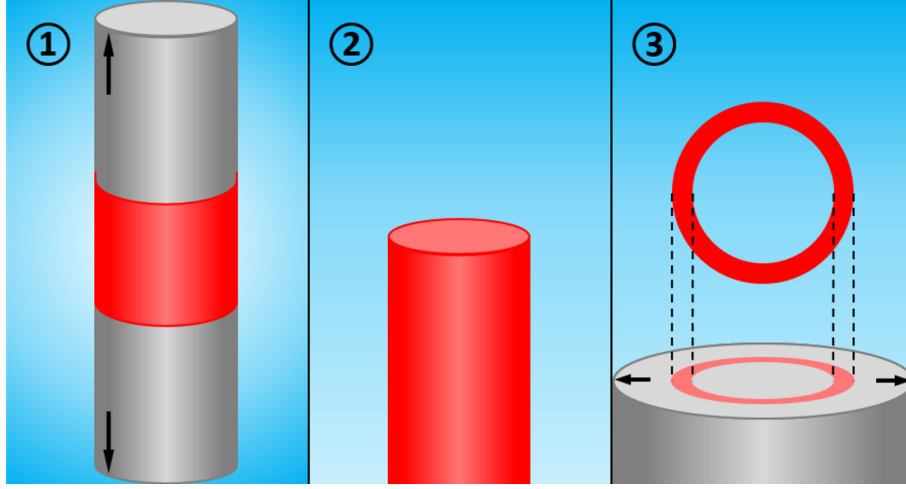


Figure 1: Illustrations of the models investigated: ① the ‘annular band’ electrode model, ② the cylinder electrode model, ③ the ‘embedded ring’ electrode model. The black arrows in the figures represent infinitely expanding insulating areas.

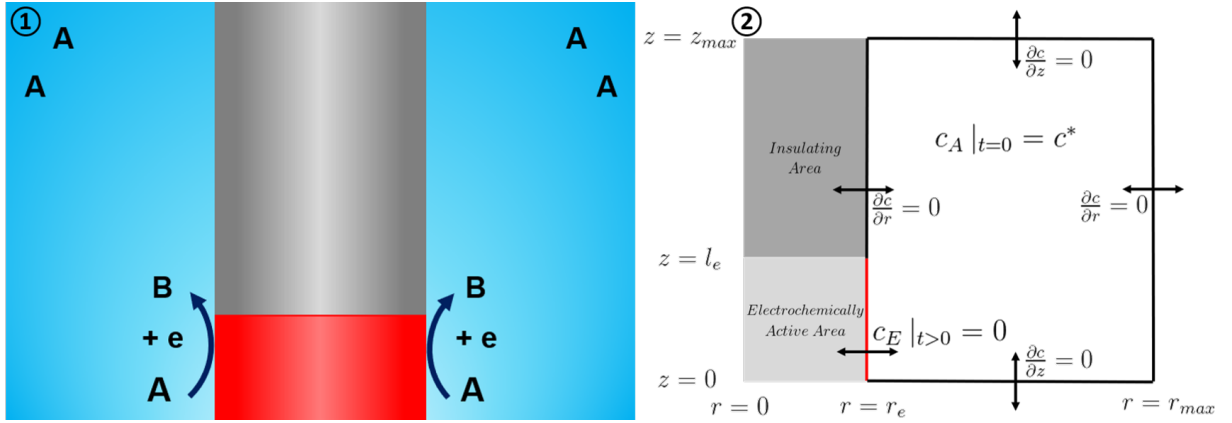


Figure 2: Cross-sectional illustration (left) and boundary conditions (right) of the ‘annular band’ electrode model. c is the concentration of the analyte A for a certain space point, c_A is the concentration of the analyte A for all of the points in the model, c^* is the initially uniform concentration of the analyte A , c_E is the concentration of the analyte A for points at the surface of the electrochemically active area, r_{max} and z_{max} are the boundaries of the simulated space in the z - and r -axis, l_e is the length of the annular band in the z -axis.

concentration profiles are recorded and subsequently investigated after applying the overpotential.

2.1.1 The ‘Annular Band’ Electrode Model

In this model, as illustrated in Figure ① in Figure 2, there is an infinitely long insulating cylinder with radius r_e in a solution of the analyte A with an electrochemically active area with length l_e . The area shown in grey is insulated and the electrochemically active area is shown in red. The analyte A is shown in blue.

This system is modelled in cylindrical coordinates (r, z, ϕ) , where r is the radial distance, z is the axial distance, and ϕ is the angle around the z -axis of the plane set by the r -axis and the z -axis. The mass transport can be described by the diffusion equation:

$$\frac{\partial c}{\partial t} = D\nabla^2 c = D\left(\frac{\partial^2 c}{\partial r^2} + \frac{1}{r}\frac{\partial c}{\partial r} + \frac{\partial^2 c}{\partial z^2} + \frac{1}{r^2}\frac{\partial^2 c}{\partial \phi^2}\right) \quad (1)$$

There is a rotational symmetry around the z -axis in this model; the concentration at a certain point for a specific combination of r and z is independent of the angle ϕ . Therefore, a simplification of the three-dimensional coordinate system (r, z, ϕ) to a two-dimensional coordinate system (r, z) can be made and the diffusion equation here and in all following models can be simplified to:

$$\frac{\partial c}{\partial t} = D\left(\frac{\partial^2 c}{\partial r^2} + \frac{1}{r}\frac{\partial c}{\partial r} + \frac{\partial^2 c}{\partial z^2}\right) \quad (2)$$

The spatial boundary conditions for the potential step experiment are shown on the right side figure in Figure 2. The initial concentration of A in solution is set to c^* :

$$t = 0, \quad r_e \leq r \leq r_{max}, \quad 0 \leq z \leq z_{max} : \quad c = c^* \quad (3)$$

For $t > 0$, the boundary condition at the electrochemically active area shown in red corresponds to a potential step applied at $t = 0$ from a potential at which no current flows to one where there is a diffusion-controlled current flowing:

$$t > 0, \quad r = r_e, \quad 0 \leq z \leq l_e : \quad c = 0 \quad (4)$$

No-flux boundaries are set everywhere else:

$$\left\{ \begin{array}{ll} t > 0, & r = r_e, \quad l_e < z \leq z_{max} : \quad \frac{\partial c}{\partial r} = 0 \\ t > 0, & r = r_{max}, \quad 0 \leq z \leq z_{max} : \quad \frac{\partial c}{\partial r} = 0 \\ t > 0, & z = 0, \quad 0 \leq r \leq r_{max} : \quad \frac{\partial c}{\partial z} = 0 \\ t > 0, & z = z_{max}, \quad 0 \leq r \leq r_{max} : \quad \frac{\partial c}{\partial z} = 0 \end{array} \right. \quad (5)$$

where it is worth noting that the simulation space is determined by the total simulation time t_{sim} as:

$$\begin{cases} r_{max} = r_e + x_{sim} \\ z_{max} = l_e + x_{sim} \\ x_{sim} = 6\sqrt{Dt_{sim}} \end{cases} \quad (6)$$

where the x_{sim} is set in a way that the simulation space is large enough so that concentration changes at the electrode are not affected by the boundaries at the far ends³³.

Following Fick's first law and Faraday's law, we can calculate the current responses for the 'annular band' electrode model as:

$$I_s = Fj_s \quad \text{where} \quad j_s = -2\pi D \int_0^{l_e} \left. \frac{\partial c}{\partial r} \right|_{r=r_e} r_e dz \quad (7)$$

where I_s is the current to the side of the cylinder, F is the Faraday constant, and j_s is the flux of the analyte A to the side of the cylinder.

2.1.2 The Cylinder Electrode Model

As shown in Figure ① of Figure 3, the 'full cylinder' electrode model is described via the radius and the length of the cylinder, r_e and l_e . The side and the end of this cylinder are electrochemically active resembling a wire electrode, which is commonly used in experiments. In order to investigate the electrochemical reactions at the side and the end of the cylinder electrode, we introduce two additional limiting models, the 'side-active-only cylinder' electrode model, and the 'end-active-only cylinder' electrode model, where the end or the side, respectively, are set as an insulating area while keeping other model parameters unchanged, as shown in Figure ② and Figure ③ of Figure 3. In all cylinder electrode models, diffusion equation is expressed by Equation 2.

Since these three models differ only in the electrochemically active areas, the boundary conditions, shown in Figure ④ in Figure 3, can be illustrated using a single figure noting that the electrochemically active boundaries and no-flux boundaries differ in three models. The concentration for all of the points in the simulations of these three models is initially set as c^* as in Equation 3 except that the points within the electrode are excluded from the simulations and the concentration for those points are set to be 0:

$$t = 0, \quad 0 \leq r < r_e, \quad 0 \leq z < l_e : \quad c = 0 \quad (8)$$

No-flux boundaries are set similarly to Equation 5. The differences in the boundary conditions among the cylinder electrode models and compared with the 'annular band' electrode model are as following:

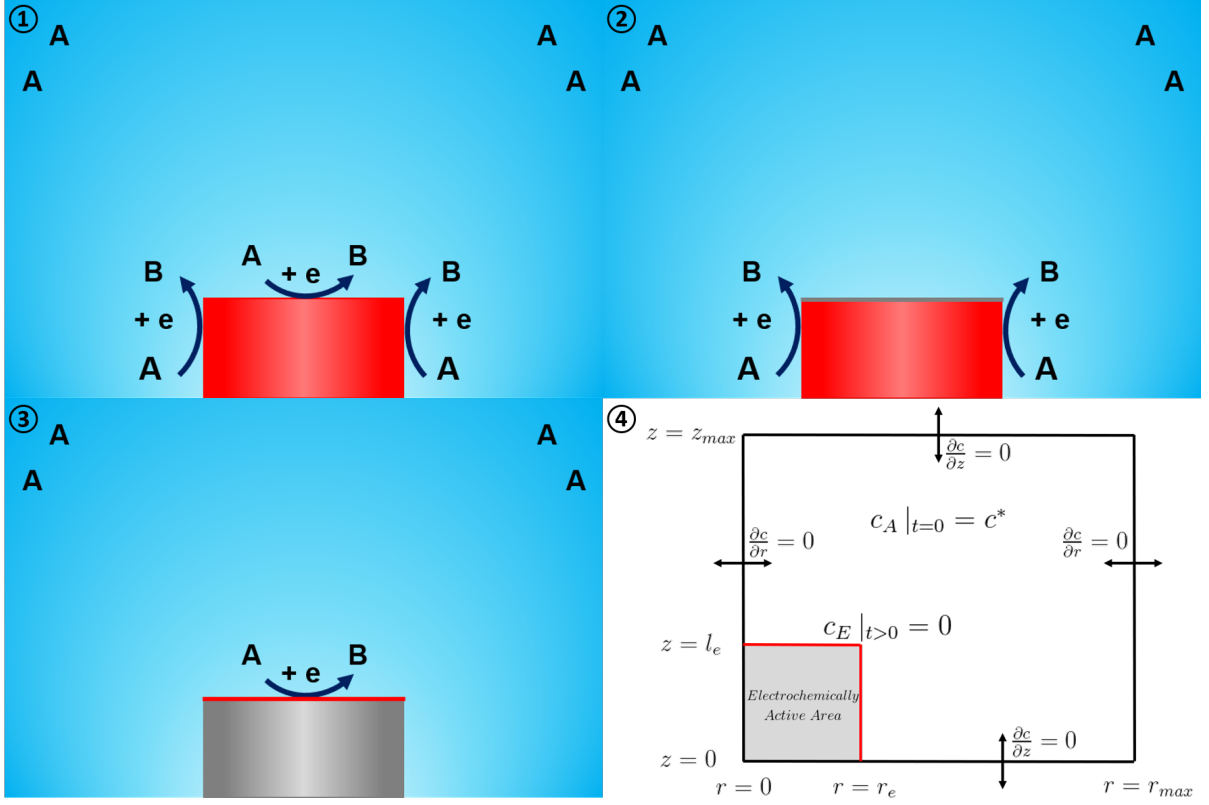


Figure 3: Cross-sectional illustrations of three electrode models: the ‘full cylinder’ electrode model (①), the ‘side-active-only cylinder’ electrode model (②), and the ‘end-active-only cylinder’ electrode model (③); boundary conditions (④) of these three models. r_e is the radius of the electrode.

For the ‘full cylinder’ electrode model:

$$\begin{cases} t > 0, & r = r_e, 0 \leq z \leq l_e : & c = 0 \\ t > 0, & z = l_e, 0 \leq r \leq r_e : & c = 0 \end{cases} \quad (9)$$

For the ‘side-active-only cylinder’ electrode model:

$$\begin{cases} t > 0, & r = r_e, 0 \leq z \leq l_e : & c = 0 \\ t > 0, & z = l_e, 0 \leq r \leq r_e : & \frac{\partial c}{\partial z} = 0 \end{cases} \quad (10)$$

For the ‘end-active-only cylinder’ electrode model:

$$\begin{cases} t > 0, & r = r_e, 0 \leq z \leq l_e : & \frac{\partial c}{\partial r} = 0 \\ t > 0, & z = l_e, 0 \leq r \leq r_e : & c = 0 \end{cases} \quad (11)$$

where the simulation space is:

$$\begin{cases} r_{max} = r_e + x_{sim} \\ z_{max} = l_e + x_{sim} \\ x_{sim} = 6\sqrt{Dt_{sim}} \end{cases} \quad (12)$$

There are only two means of current calculation needed, i.e. the currents towards the side and the end of the cylinder. For the current towards the side of the cylinder, the calculation follows Equation 7. The current towards the end of the cylinder can be calculated as:

$$\begin{cases} I_s = Fj_s & \text{where } j_s = -2\pi D \int_0^{l_e} \frac{\partial c}{\partial r} \Big|_{r=r_e} r_e dz \\ I_e = Fj_e & \text{where } j_e = -2\pi D \int_0^{r_e} \frac{\partial c}{\partial z} \Big|_{z=l_e} r dr \\ I_t = I_s + I_e \end{cases} \quad (13)$$

where I_e is the current to the end of the cylinder, j_e is the flux of the analyte A to the end of the cylinder, and the total current I_t for the ‘full cylinder’ model is the sum of the current towards the side I_s and the end I_e of the electrode. The current responses in the ‘side-active-only cylinder’ electrode model and the ‘end-active-only cylinder’ electrode model are I_s and I_e , respectively.* We will later investigate in the different diffusion fields on these three models with different electrode geometries by varying the length l_e for a constant r_e .

2.1.3 The ‘Embedded Ring’ Electrode Model

As depicted in Figure ① in Figure 4, this model features an electrochemically active ring area enclosing an insulating circular area and surrounded by an infinite, flat, insulating area. The diffusion equation adopted in this model is Equation 2.

The boundary conditions can be found in Figure ② in Figure 4, where the outer radius of the ring area is the sum of the radius of the insulating area r_0 and the width of the ring area r_e . The initial concentration of all points and the no-flux boundaries are set as in Equation 3 and Equation 5. On the surface where the electrochemically active ring embedded, the boundary conditions are:

$$\begin{cases} t > 0, & z = 0, 0 \leq r < r_0 : & \frac{\partial c}{\partial r} = 0 \\ t > 0, & z = 0, r_0 \leq r \leq r_0 + r_e : & c = 0 \\ t > 0, & z = 0, r_0 + r_e < r \leq r_{max} : & \frac{\partial c}{\partial r} = 0 \end{cases} \quad (14)$$

*We note that the simulations for these three models are separate. For example, I_s in the ‘full cylinder’ model is different from the I_s in the ‘side-active-only cylinder’ electrode model.

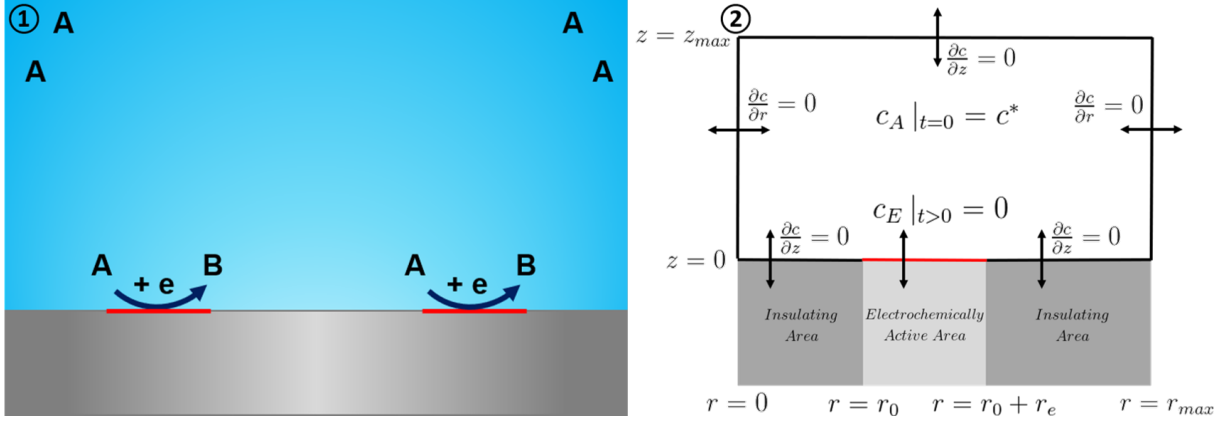


Figure 4: Cross-sectional illustration (①) and boundary conditions (②) of the ‘embedded ring’ electrode model. r_0 is the radius of the insulating area and the inner radius of the ring area, r_e is the width of the ring area.

where the simulation space is:

$$\begin{cases} r_{max} = r_0 + r_e + x_{sim} \\ z_{max} = x_{sim} \\ x_{sim} = 6\sqrt{Dt_{sim}} \end{cases} \quad (15)$$

The current can be calculated as:

$$I_r = Fj_r \quad \text{where} \quad j_r = -2\pi D \int_{r_0}^{r_0+r_e} \left. \frac{\partial c}{\partial z} \right|_{z=0} r dr \quad (16)$$

where I_r is the current, and j_r is the flux of the analyte A .

2.2 Dimensionless Parameters

To present the results in a simple and universal way, dimensional parameters are converted to their dimensionless counterparts. Dimensionless results also enable a more straightforward comparison between different experimental systems. The transformations are shown in Table 1.

In dimensionless parameters, the diffusion equation Equation 2 can be rewritten as:

$$\frac{\partial C}{\partial T} = d_A \left(\frac{\partial^2 C}{\partial R^2} + \frac{1}{R} \frac{\partial C}{\partial R} + \frac{\partial^2 C}{\partial Z^2} \right) \quad (17)$$

where C is the dimensionless concentration of the analyte A , and d_A is the dimensionless diffusion coefficient of the analyte A , as defined in Table 1.

Table 1: Transformation of dimensional parameters to dimensionless parameters where r_r is the reference length of the respective model, \mathbf{R} is the Universal Gas Constant, and \mathbf{T} is the temperature.

Dimensionless Parameter	Conversion
Concentration of species j	$C_j = \frac{c_j}{c^*}$
Diffusion coefficient of species j	$d_j = \frac{D_j}{D}$
Radial distance	$R = \frac{r}{r_r}$
Axial distance	$Z = \frac{z}{r_r}$
Time	$T = \frac{Dt}{r_r^2}$
Potential	$\theta = \frac{F}{RT}(E - E_f^0)$
Current	$J = \frac{I}{F r_r D c^*}$

The current calculations Equation 7, Equation 13, and Equation 16 can be rewritten as:

$$J_s = -2\pi d_A \int_0^{L_e} \left. \frac{\partial C}{\partial R} \right|_{R=1} dZ \quad (18)$$

$$\begin{cases} J_s = -2\pi d_A \int_0^{L_e} \left. \frac{\partial C}{\partial R} \right|_{R=1} dZ \\ J_e = -2\pi d_A \int_0^1 \left. \frac{\partial C}{\partial Z} \right|_{Z=L_e} R dR \\ J_t = J_s + J_e \end{cases} \quad (19)$$

$$J_r = -2\pi d_A \int_1^{R_e+1} \left. \frac{\partial C}{\partial Z} \right|_{Z=0} R dR \quad (20)$$

where L_e in Equation 18 and Equation 19 is the dimensionless length of the electrode, and R_e in Equation 20 is the dimensionless width of the electrochemically active area.

2.3 Computational Methods

Customised code was developed in *C++* for all of models reported in this work. Following the finite difference approach, we discretise partial differential equations for solution via matrix equations. The alternating direction implicit (ADI) method^{34–36} is used to convert the resulting systems of linear equations to tri-diagonal matrix equations that can be solved via the Thomas algorithm³⁷. *OpenMP* is used for the parallel computing and results are processed and visualised via Python scripts using the *NumPy* and *matplotlib* libraries. An expanding time grid is implemented for all models for better accuracy at short time scales. Further details can be found in the textbook³³.

We note that the testing and validation³⁸ of all of the models built are essential. Comprehensive

tests are reported in the Supplementary Information including convergence studies and studies of error of mass conservation.

3 Characterising Diffusion

The nature of diffusion towards the surface of an electrode can be appreciated by considering two limiting cases where electrode processes are diffusionally limited through the application of a sufficiently large overpotential. The first case is the one-dimensional linear diffusion whose current evolution is described by the Cottrell equation³⁹:

$$I_C = FAc^* \sqrt{\frac{D}{\pi t}} \quad (21)$$

where I_C is the current predicted by the Cottrell equation, A is the area of the electrode, c^* is the initial concentration of the analyte, D is the diffusion coefficient of the analyte and t is the dimensional time. In this case, the current response depends on $t^{-0.5}$:

$$I \propto t^{-0.5} \ ; \ J \propto T^{-0.5} \quad (22)$$

where J and T are the dimensionless current and time, respectively. The Cottrell equation is generally applicable at short time scales where the diffusion layer is constrained to a thin layer in the immediate proximity of the electrode surface such that the mass transport is controlled by diffusion across this layer of which the thickness expands with \sqrt{t} . Thus, the diffusion towards the electrode is linear and at short-enough time scales the Cottrell equation is applicable independent of the electrode geometry where A reflects the surface area of the electrode which might not necessarily be flat.

The second case is that of ‘steady-state’ diffusion characterised by a time-invariant, convergent diffusion towards the surface of the electrode where the current response remains constant:

$$I \propto t^0 \ ; \ J \propto T^0 \quad (23)$$

The terms, ‘steady state’ and ‘quasi-steady state’, are introduced and contrasted in this and following sections to clarify the concept of convergent diffusion towards different electrode geometries^{1;2;40}. As seen in the summary of steady-state and quasi-steady-state limiting currents for different geometries provided in the supplementary information, the convergent diffusion towards the end of the cylinder and the embedded ring corresponds to a true steady state with a limiting current being constant^{41–43}, whereas

the convergent diffusion towards the side of a cylindrical electrode corresponds to a quasi-steady state with a limiting current dependent of time though the currents vary extremely slowly in the long-time limits^{9;11}.

By introducing a new parameter, the ‘diffusion indicator’ α , the nature of diffusion, linear versus convergent, can be described by:

$$\alpha = 2 \frac{d(\log J)}{d(\log T)} + 1 \quad (24)$$

which is a parameter based the exponent of the time dependence of the current evolution. The two limiting cases form the lower and upper boundaries of the α value:

$$\begin{cases} \alpha = 0 & \text{for linear diffusion} \\ \alpha = 1 & \text{for convergent diffusion} \end{cases} \quad (25)$$

To demonstrate the application of the ‘diffusion indicator’ α , we consider an example of the diffusion-limited chronoamperometric current responses at a micro-disk electrode. The temporal evolution of current is described by the Shoup-Szabo equation⁴²:

$$\begin{cases} |I_{ShSz}| = 4Fr_e c^* D f(\tau) & \text{where } \tau = 4T \\ f(\tau) = 0.7854 + 0.8863\tau^{-0.5} + 0.2146 \exp(-0.7823\tau^{-0.5}) \end{cases} \quad (26)$$

where I_{ShSz} is the current predicted by the Shoup-Szabo equation, T is the dimensionless time, and r_e is the radius of the electrode.

As shown in ① in Figure 5, the electrode area is shown in red and the temporal evolution of the currents and the α values in the Shoup-Szabo equation and the Cottrell equation are plotted in ② and ③ in Figure 5, respectively. The current evolution of the Shoup-Szabo equation clearly shows that at short time scales it follows the Cottrell equation followed by a transition from the linear diffusion to convergent diffusion over time. The α curve reflects this finding with its value evolving from linear diffusion ($\alpha = 0$) to convergent diffusion ($\alpha = 1$).

In the following we use α to characterise the nature of the diffusion to a cylindrical electrode where, in particular, it can distinguish between the time responses of the cylinder side and the cylinder end.

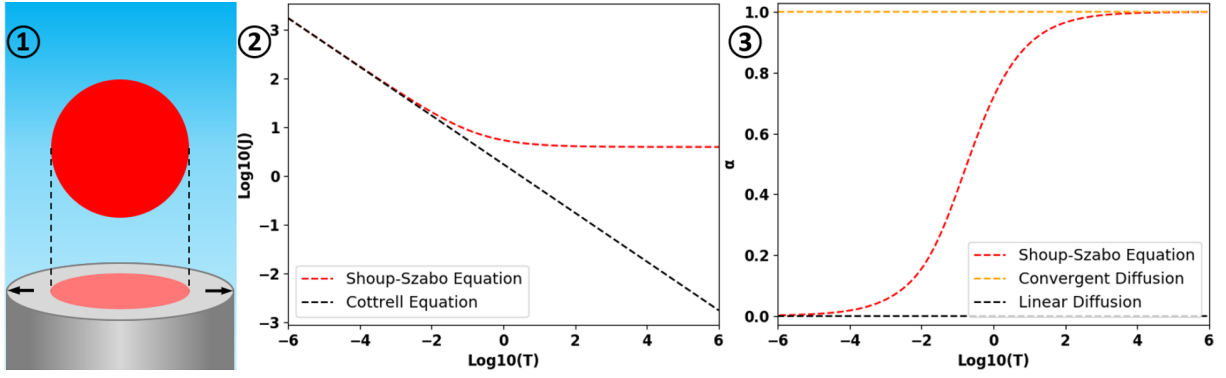


Figure 5: Example of the application of the diffusion indicator at a micro-disc electrode: ① illustration of a micro-disc electrode where the red area is the electrochemically active area, ② the temporal current evolution of the Shoup-Szabo equation (red dashed line) and the Cottrell equation (black dashed line), ③ the temporal evolution of α of the Shoup-Szabo equation (red dashed line) compared with two limiting cases: convergent diffusion (orange dashed line) and linear diffusion (black dashed line).

4 Results and Discussion

The following section reports and discusses simulation results for different geometries in the order in which the respective models were introduced. The ‘annular band’ electrode model, the ‘full cylinder’ electrode model, the ‘side-active-only cylinder’ electrode model, and the ‘end-active-only cylinder’ electrode model are addressed first and the diffusion towards the side and the end of a cylindrical electrode are analysed. Subsequently, the ‘embedded ring’ electrode model is discussed to further investigate and enlighten related diffusion processes and to establish analogies among the models.

For clarity in the following discussion, different zones are named as shown in Figure 6. In the ‘annular band’ electrode model, the zones A and E are the insulating body of the cylinder on which the electrode is mounted and the electrode, respectively, while the zones B and C are in solution. For the cylinder electrode models, the zone E is the electrode and the zones A , B and C are in solution. In the ‘embedded ring’ electrode model, the zones E and S are the electrode and the insulating substrate, respectively, while the zones I , II , and III are in solution.

4.1 The ‘Annular Band’ Electrode Model

Simulations were computed for various lengths L of the electrochemically active area while the cylinder radius was kept constant and set to a reference length r_r as defined in the dimensionless coordinates. The temporal evolution of the dimensionless currents J for four representative simulations are normalised by the lengths L and presented on the left in Figure 7 (Note the Log_{10} scales). For reasons that will be apparent below, the α values of the currents for different L are shown on the right in Figure 7.

To rationalise the simulated currents and their α values, we compare the simulated data with the Cottrell Equation and two approximate equations, which describe the temporal evolution of current in the chronoamperometry of an infinitely long cylindrical electrode. The first one was reported by Aoki et al.⁸, Equation 27:

$$\begin{cases} I_A = \frac{FDc^*}{r_e} f(T) \\ f(T) = \frac{1}{\sqrt{\pi T}} + 0.422 - 0.0675 \text{Log}_{10}T \pm 0.0058(\text{Log}_{10}T - 1.47)^2 \\ \pm \rightarrow \begin{cases} + & \text{when } \text{Log}_{10}T \geq 1.47 \\ - & \text{when } \text{Log}_{10}T < 1.47 \end{cases} \end{cases} \quad (27)$$

where I_A is the current, D is the diffusion coefficient of the analyte, c^* is the initial concentration of the analyte, T is the dimensionless time, and r_e is the radius of the electrode. The error of this equation was reported⁸ to be less than 1% for $\text{Log}_{10}T \leq 6$.

The second equation was reported by Szabo et al.¹¹, Equation 28:

$$\begin{cases} I_{Sz} = \pi F D c^* l \cdot f(T) \\ f(T) = \frac{e^{-\sqrt{\pi T}/10}}{\sqrt{\pi T}} + \frac{1}{\ln[\sqrt{4T}e^{-\gamma} + e^{5/3}]} \end{cases} \quad (28)$$

where I_{Sz} is the current, γ ($= 0.5772\dots$) is the Euler's Constant, and l is the length of the electrode. The error of this equation was reported¹¹ to be less than 1.3% for all times.

As shown in ① in Figure 7, the normalised currents and the currents predicted by the Aoki equation and the Szabo equation follow the Cottrell equation at short time scales. At long time scales, all simulated currents and currents predicted by the Aoki equation and the Szabo equation converge to a quasi-steady

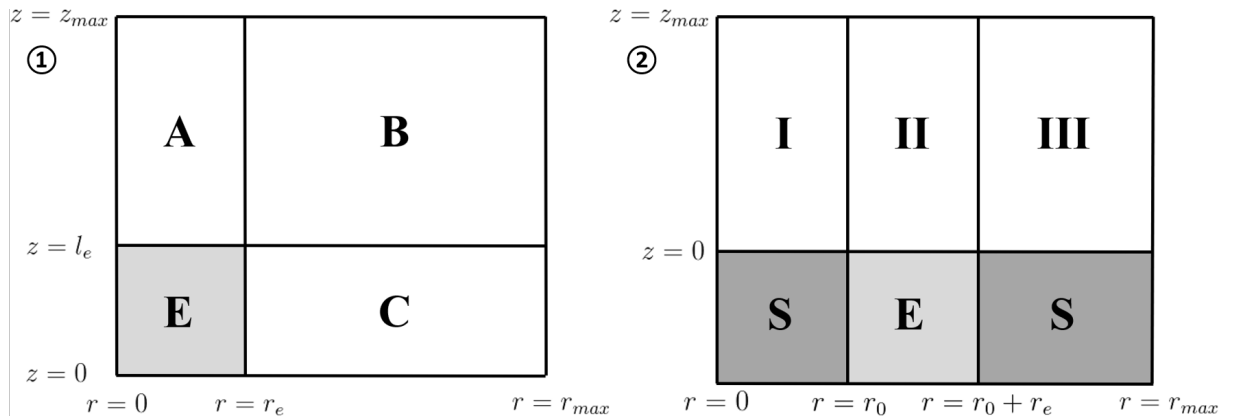


Figure 6: Different zones in the ‘annular band’ electrode model, the cylinder model (①) and the ‘embedded ring’ model (②).

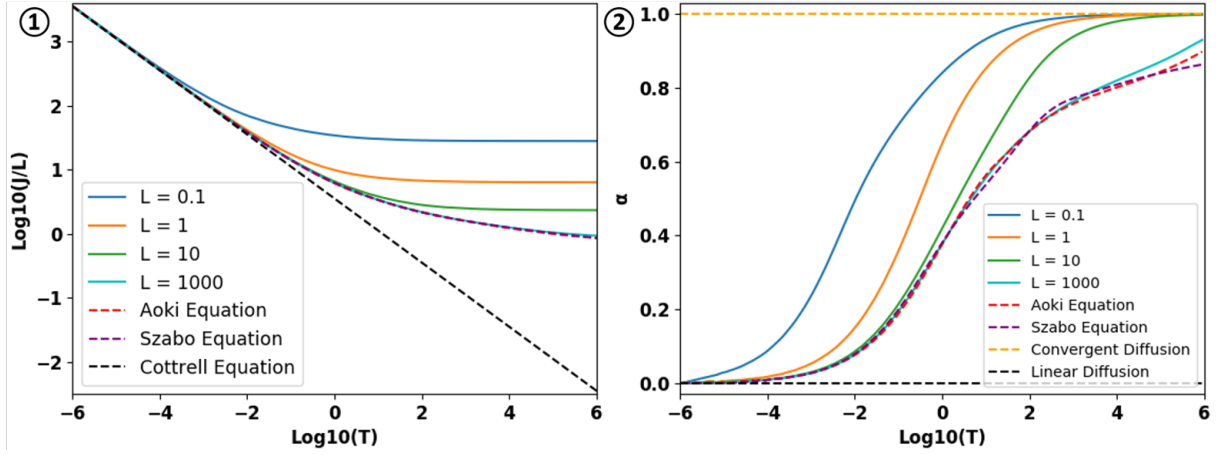


Figure 7: Temporal evolution of the normalised currents (left) and α (right) for the ‘annular band’ electrode model for different L compared with the Cottrell equation, the Aoki equation, and the Szabo equation. The simulated results are shown in solid lines: $L = 0.1$ (blue), $L = 1$ (orange), $L = 10$ (green), and $L = 1000$ (cyan). The equations to compare are shown in dashed lines: the Aoki equation (red), the Szabo equation (purple), the Cottrell equation (linear diffusion, black), and convergent diffusion (yellow).

state, where the α value is 1 in the long-time limit. For the simulated currents, the longer is the length of the electrochemically active area, the later does the current converge to a quasi-steady state, the smaller is the dimensionless quasi-steady state current, and the closer the current transient converges to the Aoki equation and the Szabo equation.

As illustrated in ② in Figure 7, the α values of all the simulated currents and those predicted by the Aoki equation and the Szabo equation reflect that the mass transport is characterised by linear diffusion at short time scales and convergent diffusion in the long-time limit with a transition in between. The α curves of the simulated current for electrodes of longer L converge to a quasi-steady state later and closer to α curves predicted by the Aoki equation and the Szabo equation. These observations reflect that the radial mass transport from the diffusion zone B contributes proportionally less to the overall current at longer L .

Additionally as shown in Figure 8, as L increases further, the two approximate equations perform well in the time range between $\text{Log}_{10}T = -6$ and $\text{Log}_{10}T = 6$ as the percentage differences between the simulated currents and the currents predicted by the Aoki equation and the Szabo equation are smaller than 1.2 in the simulated time ranges. The percentage differences are close to the errors reported by Aoki et al.⁸ and Szabo et al.¹¹.

The comparison between the simulated currents for the ‘annular band’ electrode model for different L and the currents predicted by the Aoki equation and the Szabo equation are illustrated separately in Figure 9. Together with Figure 7 and Figure 9, we find that although the currents predicted by the Aoki

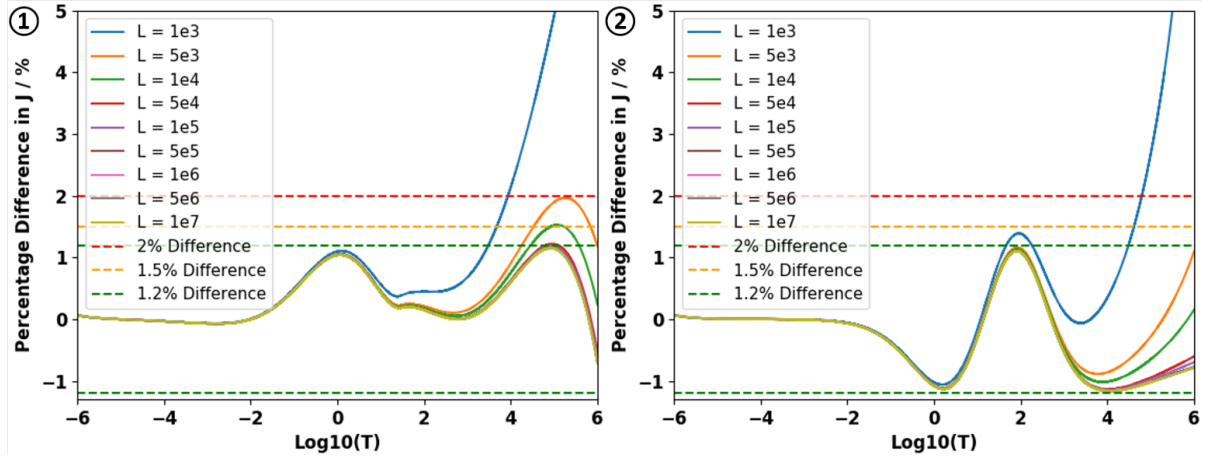


Figure 8: Percentage differences between simulated currents for the ‘annular band’ electrode model for different L compared with the Aoki equation and the Szabo equation (① and ②, respectively). The simulated results are shown in solid lines from $L = 1e3$ (blue) to $L = 1e7$ (yellow-green). Several constant percentage differences are shown in dashed lines: 1.2% (green), 1.5% (yellow), and 2.0% (red) as guidances.

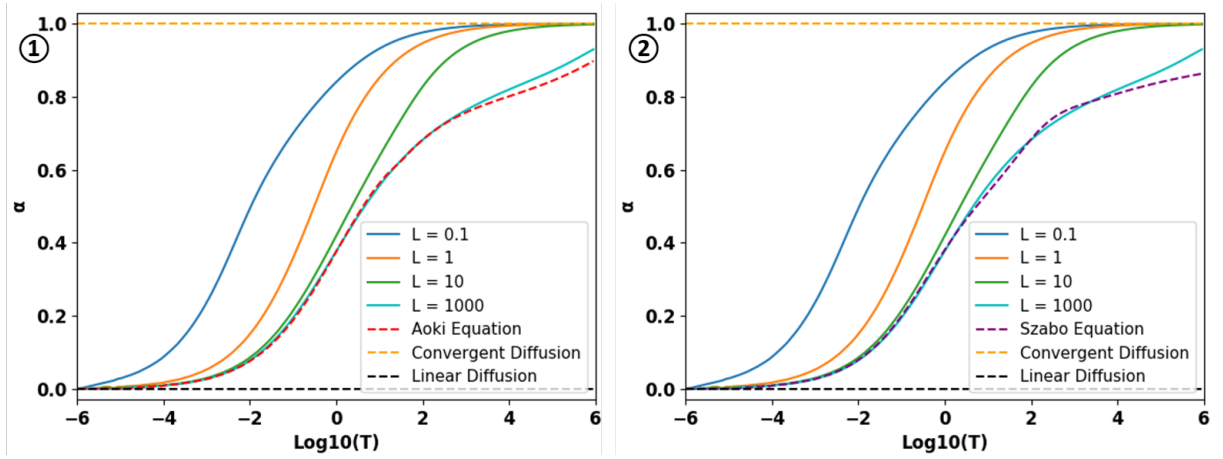


Figure 9: Temporal evolution of α for the simulated currents for the ‘annular band’ electrode model for different L compared with the Aoki equation and the Szabo equation (① and ②, respectively). The simulated results are shown in solid lines: $L = 0.1$ (blue), $L = 1$ (orange), $L = 10$ (green), and $L = 1000$ (cyan). The equations to compare are shown in dashed lines: the Aoki equation (red), the Szabo equation (purple), the Cottrell equation (linear diffusion, black), and convergent diffusion (yellow).

equation and the Szabo equation are close, there are some differences in their α plots: the Aoki equation describes the temporal evolution of simulated currents better in terms of α for longer L , especially in the time range of $\text{Log}_{10}T \leq 4$. Therefore, we will focus on the comparison between the simulated currents towards the side of the cylinder and the Aoki equation in the following sections.

4.2 The Cylinder Electrode Model

This section address the results for different cylinder electrode models.

4.2.1 The ‘Full Cylinder’ Electrode Model

Figure 10 presents simulated chronoamperograms and corresponding plots of α values for the ‘full cylinder’ electrode model evaluated for $L = 0.1, 1, 10, 1000$. In each plot the currents to the side, J_s , and to the end of the cylinder, J_e , are depicted separately and summed up to give the total current J_t .

As shown in plots on the left side in Figure 10, for shorter L , J_e is higher than J_s . As L increases, J_e remains at a similar level, J_s increases, and J_s contributes proportionally more to J_t . Whilst the many transients in the plots of currents in Figure 10 look superficially similar, the diffusion indicator α newly introduced above can be used to sensitively identify subtle differences in the transients and to track the origins of those to the different parts of the electrode via comparison with the contributions from the end and side plotted in isolation.

In plots on the right side in Figure 10, the temporal evolutions of the α values of J_t , J_s and J_e start from 0 at short time scales and converge to 1 in the long-time limit, which echoes the findings of the transition from linear to convergent diffusion. Furthermore, at short L , e.g. $L = 0.1$, the α value for J_s begins the transition from 0 to 1 earlier than those for J_t and J_e while the α values for J_t are closer to those for J_e . With increasing L , the α values for J_s begin the transition later while the differences between the α values of J_t and J_s decrease. In extreme cases, as shown in Figure 10, the plots of α against $\text{Log}_{10}T$ show stepped behaviours with two contributions, each with a characteristic ‘time constant’. Each ‘step’ is associated with a diffusion to or from a physically different part of the electrode.

The plots of α provide the insight into the diffusion mechanisms prevalent in the chronoamperograms and enable further studies. For $L = 0.1$, the α value for J_s begins the transition at around $\text{Log}_{10}T = -5$ while that for J_e begins at around $\text{Log}_{10}T = -4$. This observation can be assigned to the fact that the diffusion from the diffusion zone B contributes proportionally more to J_s at these time scales. The slope of the α values for J_s decreases around $\text{Log}_{10}T = -1$, from which we infer that there is a flux of analyte from the zones C and B towards the partially depleted zone A . When $L = 1$, the shapes of the α plots for J_s and J_e are similar, which shows that the diffusion mechanisms of the end and the side are similar for $L = 1$ though the area of the end is twice as big as that of the side which leads to different magnitudes of currents for J_s and J_e . For longer L , the α value of J_s increases more slowly to convergent diffusion which can be assigned to the proportionally smaller mass transport from zones A and B to the side of the cylinder. Furthermore, the α value of J_e increases more slowly for $\text{Log}_{10}T \geq 0$ due to the competition

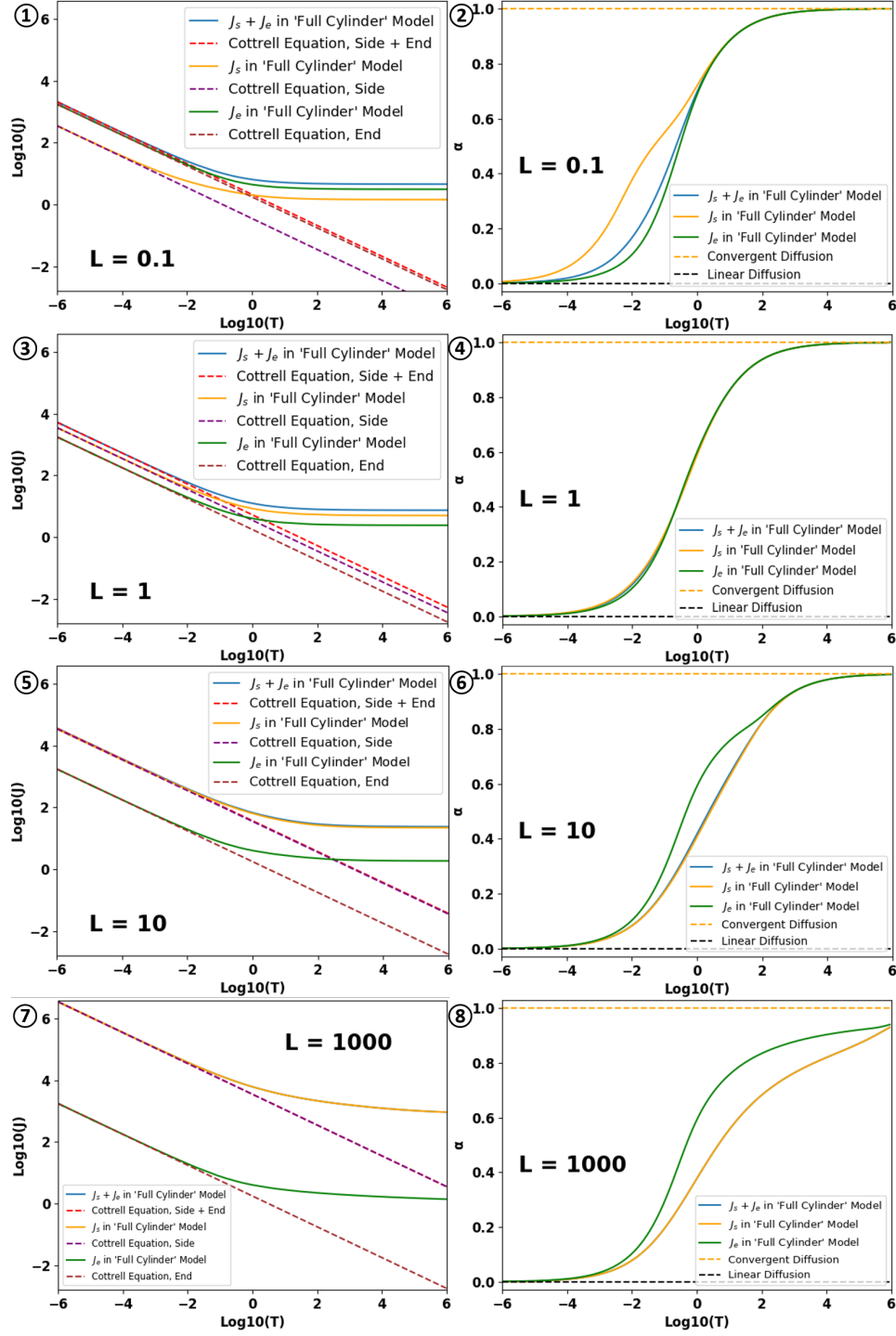


Figure 10: Temporal evolution of currents (left) and the α values (right) for the 'full cylinder' electrode model for different L compared with the Cottrell equation. The simulated results are shown in solid lines: J_t ($J_s + J_e$, blue), J_s (orange), and J_e (green). The equations to compare are shown in dashed lines: the current curves predicted by Cottrell equation for corresponding areas (red, purple, and brown), linear diffusion (black) and convergent diffusion (orange).

from the side. Finally, since J_t is the sum of J_s and J_e , the α values of J_t are closer to those of J_e when L is small. If L is long, e.g. $L = 1000$, the contribution from J_s is so large that we hardly see any difference between J_t and J_s in the α values.

The data shows L has a huge impact on the diffusion mechanisms to both the side and the end of a cylinder electrode. However, as the analysis of J_t , J_s and J_e in the ‘full cylinder’ electrode model is not sufficient to exhaustively understand the diffusion mechanisms to the side and the end, the following comparison with other simulation models is done to provide further details.

4.2.2 Currents at the Side of a Cylinder

To investigate the roles of the side and the end of a cylinder electrode in the chronoamperometry individually, we performed simulations for equal L for both the ‘side-active-only cylinder’ electrode model and the ‘end-active-only cylinder’ electrode model and compare J_s and J_e with simulated and predicted currents for other models and the equations presented below. In terms of J_s , we compare currents and α values for J_s for the ‘side-active-only cylinder’ electrode model with J_s for the ‘full cylinder’ electrode model, J_s for the ‘annular band’ electrode model, the Cottrell equation, and the Aoki equation for various $L = 0.1, 1, 10, 1000$ in Figure 11.

As shown in plots in Figure 11, the currents towards the side of the cylinder and their α values for three models and the the Aoki equation show the trends from linear-diffusion-controlled electrochemical processes at the short-time scales to quasi-steady states at the long-time scales, analogous to these trends illustrated in former sections. Furthermore, there are some stepped behaviours showing in the α plots which will be discussed later in this section.

In the current plots in Figure 11, for shorter L , the quasi-steady-state currents for J_s of these three models are in the order as, from high to low, J_s for the ‘side-active-only cylinder’ electrode model, J_s for the ‘annular band’ electrode model, J_s for the ‘full cylinder’ electrode model. The quasi-steady-state current of J_s for the ‘side-active-only cylinder’ electrode model is higher than that for the ‘annular band’ electrode model, which can be assigned to additional diffusion for the diffusion zone A . The quasi-steady-state current of J_s for the ‘full cylinder’ electrode model is lower than those for the previous two models, which we assign to the competition with the end of the cylinder. As L increases, the magnitude relationship of simulated currents remains the same while the simulated currents decrease and approach to the Aoki equation. We infer that the decline in simulated currents as L increases may be caused by the proportionally less contribution of the diffusion zone A and B to the overall mass transport towards the side of the cylinder.

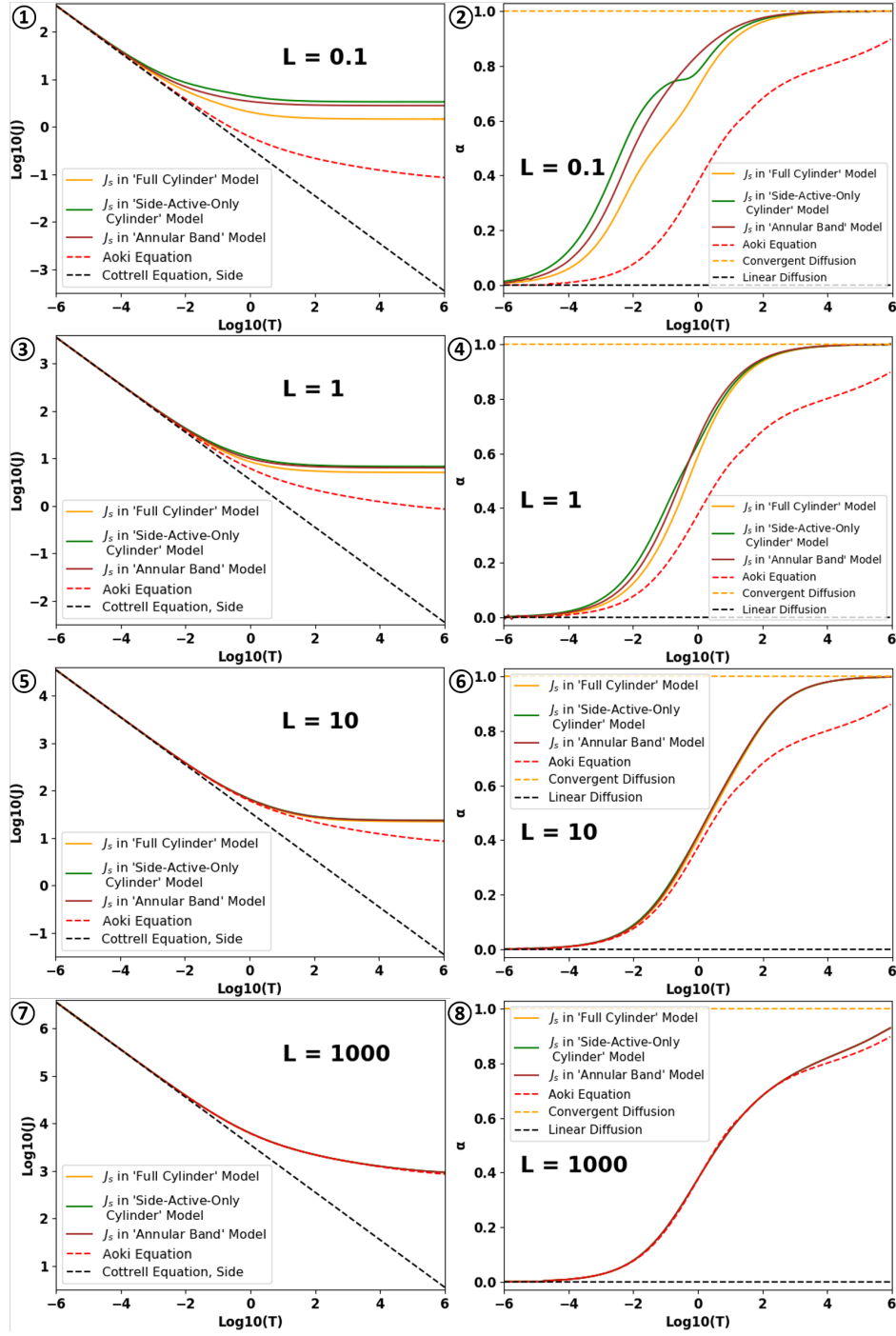


Figure 11: Temporal evolutions of currents (left) and the α values (right) for the 'side-active-only cylinder' electrode model for different L compared with simulated currents and the α values for other models, the Cottrell equation and the Aoki equation. The simulated results are shown in solid lines: J_s in 'full cylinder' model (orange), J_s in 'side-active-only cylinder' model (green), and J_s in 'annular band' model (brown). The equations to compare are shown in dashed lines: the Aoki equation (red), the Cottrell equation (linear diffusion, black), and convergent diffusion (yellow).

We can study the diffusion towards the side of a cylinder further by analysing the α plots. In the α plots in Figure 11, for $\text{Log}_{10}T < -2$, the slopes of the α plots for three models are in the same order, from high to low, as the magnitude relationship of their corresponding simulated currents, which we assign to the contribution from diffusion zone A for the ‘side-active-only cylinder’ electrode mode and the competition from the end of the cylinder for the ‘full cylinder’ electrode mode. However, for $-2 \leq \text{Log}_{10}T < 0$, the α plots for J_s for the ‘side-active-only cylinder’ electrode model and the ‘full cylinder’ electrode model show stepped behaviours. The slopes of the α plots for these two models decrease for $-2 \leq \text{Log}_{10}T < 0$, which we assign to the mass transport from zones C and B to zone A . By comparing the α plots and the diffusion zones for these three models, the stepped behaviours in the α plots of J_s for the ‘side-active-only cylinder’ electrode model and the ‘full cylinder’ electrode model is caused by the diffusion from zone A ; two contributions of diffusion with two different ‘time constants’ can, therefore, only be assigned to the mass transport from zone A , and the mass transport from zone B and zone C combined. As L increases, decreasing proportional contribution from the zones A and B to the side of the cylinder results in the approach of the α plots to the Aoki equation which echo the observations in the current plots.

4.2.3 Currents at the End of Cylinder

In terms of J_e , we compare current and the α values of J_e for the ‘end-active-only cylinder’ electrode model with those of J_e for the ‘full cylinder’ electrode model, and the Cottrell equation and the Shoup-Szabo equation in Figure 12.

As shown on the left in Figure 12, for shorter L , e.g. $L = 0.1$, the steady-state current for J_e in the ‘end-active-only cylinder’ electrode model is higher than that in the ‘full cylinder’ electrode model while the steady-state current calculated via Shoup-Szabo equation is lower than the two simulated steady-state currents. As L increases, the steady state current for J_e in the ‘full cylinder’ electrode model drops dramatically while that for the ‘end-active-only cylinder’ electrode model increases slightly.

As shown on the left in Figure 12, the α values of simulated currents and current calculated by the Shoup-Szabo equation start from linear diffusion at the short time scales to convergent diffusion at the long time scales. For the shorter L , the α plot for J_e in the ‘end-active-only cylinder’ electrode model tends to converge to steady state earlier than that for the ‘full cylinder’ electrode model while the approach of the Shoup-Szabo equation to 1 is slower than those for J_e in the ‘end-active-only cylinder’ electrode model and J_e in the ‘full cylinder’ electrode model, which we assign to the contributions from the diffusion zone C . Consistent with the slower approach convergent diffusion for J_s in both models for

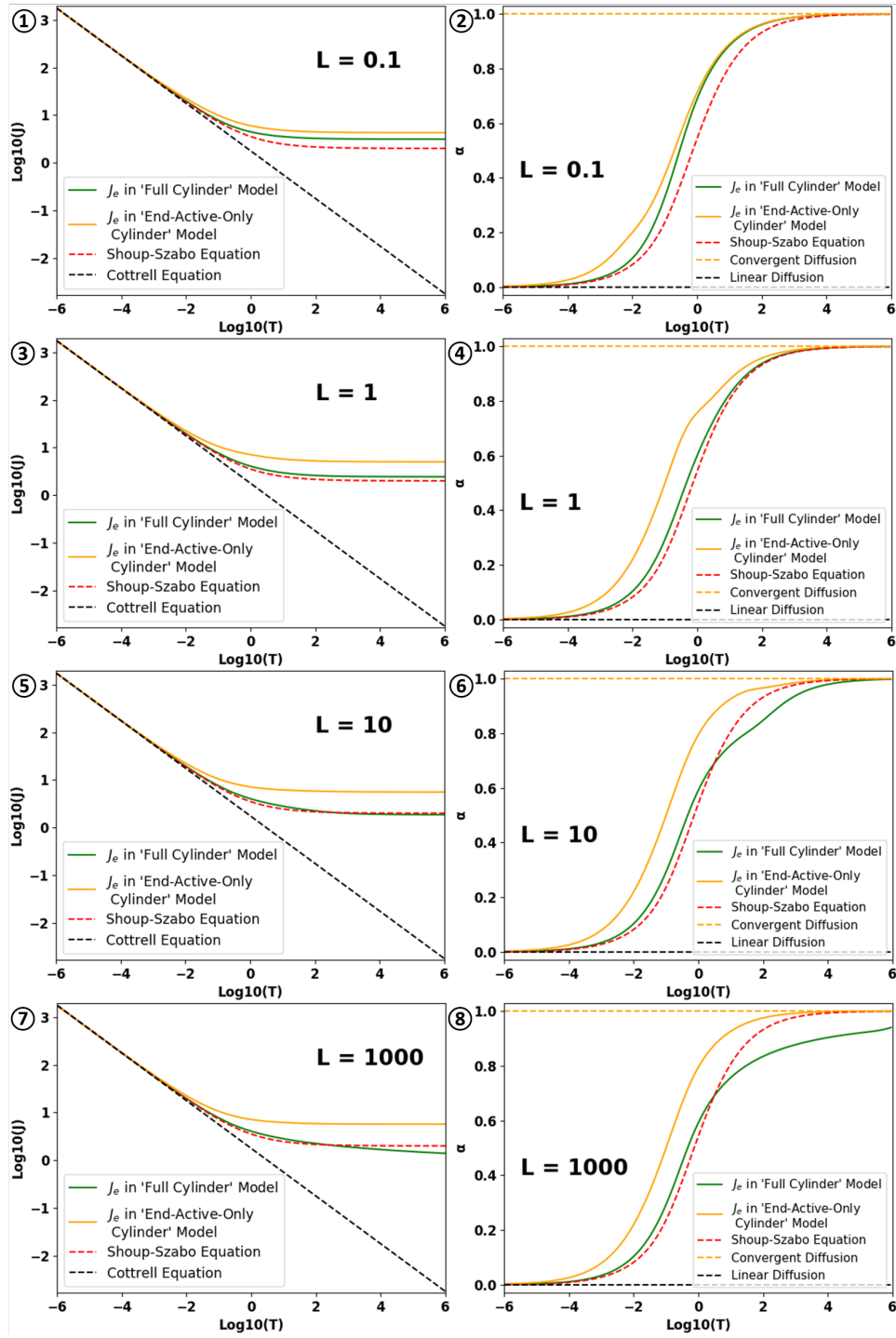


Figure 12: Temporal evolutions of currents (left) and the α values (right) for the 'end-active-only cylinder' electrode model for different L compared with simulated currents and the α values for the 'full cylinder' electrode model, the Cottrell equation and the Shoup-Szabo equation. The simulated results are shown in solid lines: J_e in 'full cylinder' model (green), and J_e in 'side-active-only cylinder' model (orange). The equations to compare are shown in dashed lines: the Shoup-Szabo equation (red), the Cottrell equation (linear diffusion, black), and convergent diffusion (yellow).

$\text{Log}_{10}T \geq -2$ shown in previous sections, the approach of the α plot for J_e for both models is faster than the microdisc electrode without zone C . As L increases, the stepped behaviours in both models shows that there is an increase of mass transport to the end of the cylinder in the ‘end-active-only cylinder’ electrode model while there is a decrease of mass transport in the ‘full cylinder’ electrode model, which we infer that for longer L the diffusion from zone C contributes to J_e in the ‘end-active-only cylinder’ electrode model more while the competition from the side of the cylinder increases for the ‘full cylinder’ electrode model, which results in larger differences in both the currents plots and the α plots between the two models.

4.3 The ‘Embedded Ring’ Electrode Model

In the previous sections, we have seen that, for shorter L , e.g. $L = 0.1$, the rates of the α plots for J_s in the ‘full cylinder’ electrode model and J_s in the ‘side-active-only cylinder’ electrode model slows down for $-2 \leq \text{Log}_{10}T < 0$ due to the diffusive flux from the zone C to the zones B and A . If L is even smaller, the electrochemically active area which adopts a band-shape for the ‘side-active-only cylinder’ electrode model that tends to resemble a ring-shaped electrode on an insulating surface as zone C decreases. Therefore, we investigate the ‘embedded ring’ electrode model to further study the observations in previous models.

In this model, we calculate data for varying widths R_e of the embedded ring. The simulated currents are then normalised by the areas of the electrodes:

$$J_{Nr} = J_r/a \quad \text{where} \quad a = \pi(R_e^2 - 1^2) \quad (29)$$

where J_{Nr} is the normalised current for the ‘embedded ring’ electrode model, a is the area of the ring-shaped electrode.

As shown in plots in Figure 13, the normalised currents towards the embedded ring and their α values also show the trends from linear-diffusion-controlled electrochemical processes at the short-time scales to quasi-steady states at the long-time scales. The larger is the area of the ring-shaped electrode, the longer it takes the current to approach to the steady state. For shorter R_e , e.g. $R_e = 0.1$, there is a drop in the approach rate for the α plot at $-2 \leq \text{Log}_{10}T < 0$, which we assign to the depletion of diffusion zone I . As R_e increases, the drop in approach rate decreases due to the smaller influence of zone I on the total current. Considering the similarities in the diffusion zones of models shown in Figure 6, these observations reflect the stepped behaviours are resulted from the different ‘time constants’ for the diffusion from zones A (I) and other zones. Furthermore, the stepped behaviours are more obvious when the zone A (I) is larger.

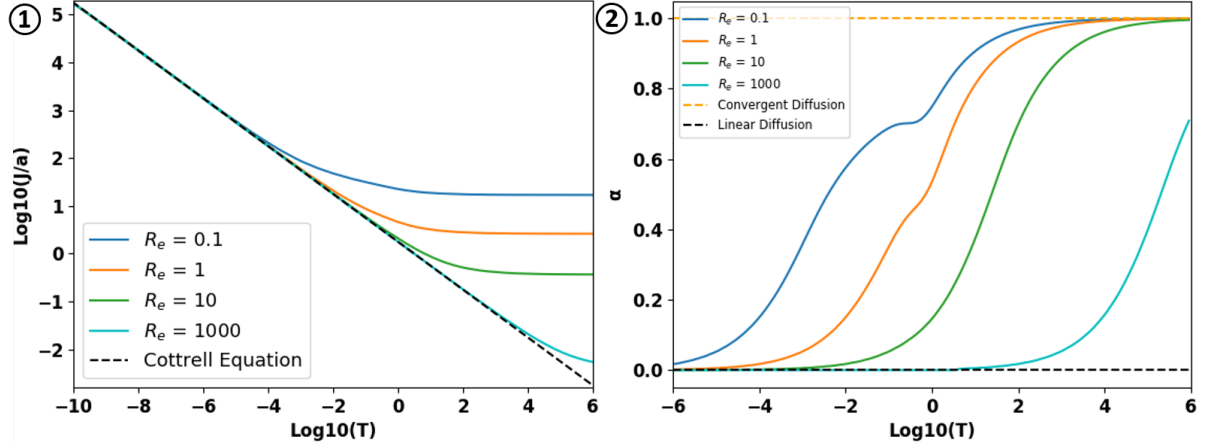


Figure 13: Temporal evolution of normalised currents (left) and the α values (right) for the ‘embedded ring’ electrode model for $R_e = 0.1, 1, 10, 1000$ compared with the Cottrell equation. The simulated results are shown in solid lines: $R_e = 0.1$ (blue), $R_e = 1$ (orange), $R_e = 10$ (green), and $R_e = 1000$ (cyan). The equations to compare are shown in dashed lines: the Cottrell equation (linear diffusion, black), and convergent diffusion (yellow).

4.4 Physical Insights

In previous sections, we reported that when L increases, J_s in the ‘annular band’ electrode model, the ‘side-active-only cylinder’ electrode model, and the ‘full cylinder’ electrode model approach to the Aoki equation. Therefore, beyond a certain value of L , we can use the the Aoki equation to predict the chronoamperometric currents in all three models.

For increasing L , we compare the simulated currents with the Aoki equation for $-6 \leq \text{Log}_{10}T \leq 6$ and obtain the percentage differences. As shown in Figure 14, the percentage differences compared with the Aoki equation in all three models are small due to little influence of the zones A and B , and the electrochemically active area at the end of the cylinder when L is large.

Here we present a case study for the typical experimental parameters shown in Table 2. By converting the dimensionless results into their dimensional forms, we produce a set of dimensional simulated results that can be used by experimentalists to obtain an insight of how the simulations relate to experiments. Shown in Figure 14 is a second x-axis showing the dimensional lengths of which the largest percentage differences between the simulated currents and the currents predicted by the Aoki equation $-6 \leq \text{Log}_{10}T \leq 6$. It is worth noting that when $L = 5 * 10^3$ ($l = 17.5\text{mm}$), where l is the dimensional length of the cylinders, the largest percentage difference between the simulated currents and the currents predicted by the Aoki equation for the ‘annular band’ electrode model, the ‘full cylinder’ electrode model and the ‘side-active-only cylinder’ electrode model are, respectively, 1.966%, 1.972%, and 1.978%. Therefore, if l is longer than 17.5mm when the radius is $3.5\mu\text{m}$, the largest percentage errors between simulated

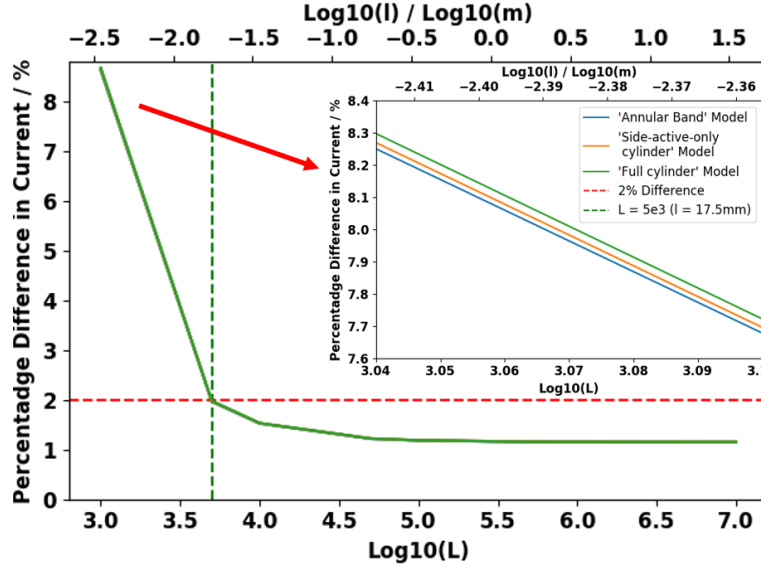


Figure 14: Percentage differences in currents between simulated currents in the ‘annular band’ electrode model, the ‘side-active-only cylinder’ electrode model, and the ‘full cylinder’ electrode model compared with the Aoki equation. The percentage differences are shown in solid lines: the ‘annular band’ electrode model (blue), the ‘side-active-only cylinder’ electrode model (orange), and the ‘full cylinder’ electrode model (green). Some reference values are shown in dashed lines: 2% (red), and $L = 5 * 10^3$ ($l = 17.5mm$) (green).

Table 2: Value of dimensional parameters commonly used in microelectrode chronoamperometric experiments^{25;27}

Dimensional parameter	Value
Electrode radius (r_e)	$3.5\mu m$
Diffusion coefficient (D)	$10^{-9}m^2/s$
Analyte initial concentration (c^*)	$1mM$

currents from three models and the Aoki equation are less than 2% for $1.225 * 10^{-8}s \leq t \leq 1.225 * 10^4s$.

5 Conclusions

This work has introduced a new indicator, the diffusion indicator α , to characterise diffusion which enables the discovery and analysis the extents of linear and convergent diffusion in chronoamperometric measurements. By using this indicator in the analysis of simulated chronoamperometric currents, the roles of different parts of the electrode surface and different diffusion zones are identified and discussed, in particular, the ‘top’ and ‘side’ of the cylinder can show different responses with different time scales leading to ‘stepped’ chronoamperometry. This work further determines the conditions under which the Aoki equation can be used to predict chronoamperometric currents for cylinder-like models. We find that

if the length of the cylinder is at least 5000 times longer than the radius, the percentage differences at different times between the simulated current and the Aoki equation are less than 2%, that is for instance, if the length of the cylinder is longer than 17.5mm when the radius is $3.5\mu\text{m}$.

References

- [1] K. Aoki. Theory of ultramicroelectrodes. *Electroanalysis*, 5(8):627–639, 1993.
- [2] J. Heinze. Ultramicroelectrodes in electrochemistry. *Angewandte Chemie International Edition in English*, 32(9):1268–1288, 1993.
- [3] R. J. Forster. Microelectrodes: new dimensions in electrochemistry. *Chem. Soc. Rev.*, 23:289–297, 1994.
- [4] R. J. C. Brown and D. J. L. Brett. Microelectrode voltammetry as a high accuracy method for determination of diffusion coefficients. *Microchimica Acta*, 164(3):337–344, 2009.
- [5] D.E. Tallman. Microelectrodes for voltammetry—a personal historical perspective. *Journal of Solid State Electrochemistry*, 15(7-8):1703–1710, 2011.
- [6] K. J. Aoki, C. Zhang, J. Chen, and T. Nishiumi. Heterogeneous reaction rate constants by steady-state microelectrode techniques and fast scan voltammetry. *Journal of Electroanalytical Chemistry*, 706:40–47, 2013.
- [7] K. J. Aoki and J. Chen. Effects of the dipolar double layer on elemental electrode processes at micro- and macro-interfaces. *Faraday Discussions*, 210:219–234, 2018.
- [8] K. Aoki, K. Honda, K. Tokuda, and H. Matsuda. Voltammetry at Microcylinder Electrodes. 2. Chronoamperometry. *Journal of Electroanalytical Chemistry*, 186(1-2):79–86, 1985.
- [9] P. M. Kovach, W. L. Caudill, D. G. Peters, and R. M. Wightman. Faradaic electrochemistry at microcylinder, band, and tubular band electrodes. *Journal of Electroanalytical Chemistry*, 185(2):285–295, 1985.
- [10] C.A. Amatore, M.R. Deakin, and M. Wightman. Electrochemical kinetics at microelectrodes part 1. quasi-reversible electron transfer at cylinders. *Journal of Electroanalytical Chemistry*, 206(1-2):23–36, 1986.

- [11] A. Szabo, D. K. Cope, D. E. Tallman, P. M. Kovach, and R. M. Wightman. Chronoamperometric current at hemicylinder and band microelectrodes: Theory and experiment. *Journal of Electroanalytical Chemistry*, 217(2):417–423, 1987.
- [12] K. Aoki and H. Kaneko. Theory of irreversible cyclic voltammograms at microcylinder electrodes. *Journal of Electroanalytical Chemistry*, 247(1-2):17–27, 1988.
- [13] S.T. Singleton, J.J. O’Dea, and J. Osteryoung. Analytical utility of cylindrical microelectrodes. *Analytical Chemistry*, 61(11):1211–1215, 1989.
- [14] B.J. Seddon, H.H. Girault, M.J. Eddowes, W. Peng, and Z. Zhao. Dual-cylinder microelectrodes. part 1.-theoretical consideration of the steady-state current. *Journal of the Chemical Society, Faraday Transactions*, 87(16):2603–2606, 1991.
- [15] W. Peng and E. Wang. Theory of steady-state current at multiple microcylinder electrodes coupled with a parallel planar electrode. *Analytical Chemistry*, 65(20):2719–2723, 1993.
- [16] R. Ferrigno, P.F. Brevet, and H.H. Girault. Finite element simulation of the chronoamperometric response of recessed and protruding microdisc electrodes. *Electrochimica Acta*, 42(12):1895 – 1903, 1997.
- [17] E. J. F. Dickinson, I. Streeter, and R. G. Compton. Theory of chronoamperometry at cylindrical microelectrodes and their arrays. *The Journal of Physical Chemistry C*, 112(31):11637–11644, 2008.
- [18] Y.-M. Fang, J.-J. Sun, and G.-N. Chen. A simple approach to the solution of the diffusion equation at the microcylinder electrode - an inspiration from the film projector. *ChemPhysChem*, 10(14):2393–2396, 2009.
- [19] E.P. Rivero, P. Granados, F.F. Rivera, M. Cruz, and I. González. Mass transfer modeling and simulation at a rotating cylinder electrode (rce) reactor under turbulent flow for copper recovery. *Chemical Engineering Science*, 65(10):3042 – 3049, 2010.
- [20] D. Britz, O. Østerby, and J. Strutwolf. Reference values of the chronoamperometric response at cylindrical and capped cylindrical electrodes. *Electrochimica Acta*, 55(20):5629–5635, 2010.
- [21] L. K. Bieniasz. A highly accurate, inexpensive procedure for computing theoretical chronoamperometric current at cylindrical wire electrodes. *Electrochimica Acta*, 56(20):6982–6988, 2011.

- [22] L. K. Bieniasz. Automatic simulation of electrochemical transients at cylindrical wire electrodes, by the adaptive huber method for volterra integral equations. *Journal of Electroanalytical Chemistry*, 662(2):371–378, 2011. cited By 13.
- [23] L. K. Bieniasz. Automatic solution of integral equations pertinent to diffusion with first order homogeneous reactions at cylindrical wire electrodes. *Journal of Electroanalytical Chemistry*, 674:38–47, 2012.
- [24] S. J. Percival and B. Zhang. Electrocatalytic reduction of oxygen at single platinum nanowires. *The Journal of Physical Chemistry C*, 117(27):13928–13935, 2013.
- [25] J. Ellison, C. Batchelor-McAuley, K. Tschulik, and R. G. Compton. The use of cylindrical micro-wire electrodes for nano-impact experiments; facilitating the sub-picomolar detection of single nanoparticles. *Sensors and Actuators B: Chemical*, 200:47 – 52, 2014.
- [26] J. Li, Q. Fang, F. Liu, and Y. Liu. Analytical modeling of dislocation effect on diffusion induced stress in a cylindrical lithium ion battery electrode. *Journal of Power Sources*, 272:121 – 127, 2014.
- [27] C. Batchelor-McAuley, J. Ellison, K Tschulik, P. L. Hurst, R. Boldt, and R. G. Compton. In situ nanoparticle sizing with zeptomole sensitivity. *Analyst*, 140:5048–5054, 2015.
- [28] J. Chakraborty, C. P. Please, A. Goriely, and S. J. Chapman. Combining mechanical and chemical effects in the deformation and failure of a cylindrical electrode particle in a li-ion battery. *International Journal of Solids and Structures*, 54:66 – 81, 2015.
- [29] H. R. Moazami, S. S. H. Davarani, J. Mohammadi, S. Nojavan, and M. Abrari. The effect of electric field geometry on the performance of electromembrane extraction systems: Footprints of a third driving force along with migration and diffusion. *Analytica Chimica Acta*, 891:151 – 159, 2015.
- [30] A. Molina, J. González, E. Laborda, and R.G. Compton. Analytical solutions for fast and straightforward study of the effect of the electrode geometry in transient and steady state voltammetries: Single- and multi-electron transfers, coupled chemical reactions and electrode kinetics. *Journal of Electroanalytical Chemistry*, 756:1 – 21, 2015.
- [31] S. Eloul, E. Kätelhön, C. Batchelor-McAuley, K. Tschulik, and R. G. Compton. Diffusional impacts of nanoparticles on microdisc and microwire electrodes: The limit of detection and first passage statistics. *Journal of Electroanalytical Chemistry*, 755:136 – 142, 2015.

- [32] K. Ngamchuea, C. Lin, C. Batchelor-McAuley, and R. G. Compton. Supported microwires for electroanalysis: Sensitive amperometric detection of reduced glutathione. *Analytical Chemistry*, 89(6):3780–3786, 2017.
- [33] R. G. Compton, E. Laborda, and K. R. Ward. *Understanding Voltammetry: Simulation of Electrode Processes*. Imperial College Press, 2014.
- [34] D. Peaceman and H. Rachford, Jr. The numerical solution of parabolic and elliptic differential equations. *Journal of the Society for Industrial and Applied Mathematics*, 3:28–41, 1955.
- [35] J. Heinze. Diffusion processes at finite (micro) disk electrodes solved by digital simulation. *Journal of Electroanalytical Chemistry and Interfacial Electrochemistry*, 124:73 – 86, 1981.
- [36] J. A. Alden and R. G. Compton. A general method for electrochemical simulations. 1. formulation of the strategy for two-dimensional simulations. *The Journal of Physical Chemistry B*, 101:8941–8954, 1997.
- [37] W. H. Press, S. A. Teukolsky, W. T. Vetterling, and B. P. Flannery. *Numerical Recipes : The Art of Scientific Computing (Third Edition)*. Cambridge University Press, 2007.
- [38] E. Kätelhön and R. G. Compton. Testing and validating electroanalytical simulations. *Analyst*, 140:2592–2598, 2015.
- [39] F. G. Cottrell. *Zeitschrift für Physikalische Chemie*, 42:385, 1903.
- [40] A. J. Bard, L. R. Faulkner, C. G. Zoski, and J. Leddy. *Electrochemical methods : fundamentals and applications*. New York ; Chichester, second edition. edition, 2001.
- [41] K. Aoki and J. Osteryoung. Diffusion-controlled current at the stationary finite disk electrode: Theory. *Journal of Electroanalytical Chemistry*, 122(C):19–35, 1981.
- [42] D. Shoup and A. Szabo. Chronoamperometric current at finite disk electrodes. *Journal of Electroanalytical Chemistry*, 140(2):237–245, 1982.
- [43] A. Szabo. Theory of the current at microelectrodes: Application to ring electrodes. *Journal of Physical Chemistry*, 91(11):3108–3111, 1987.